# Reaction-Induced Microsyneresis in Oxide-Based Gels: The Assembly of Hierarchical Microsphere Networks

Ai Du,* Bin Zhou,* Weiwei Xu, Qiujie Yu, Yang Shen, Zhihua Zhang, Jun Shen, and Guangming Wu

Shanghai Key Laboratory of Special Artificial Microstructure Materials and Technology, School of Physics Science and Engineering, Tongji University, Shanghai 200092, P. R. China

Ⓢ *Supporting Information*

ABSTRACT: Rigid and stable networks composed of litchi-shaped microspheres were formed via hierarchical self-assembly (SA) of oxide-based nanoparticles (NPs). The phenomenon of the apparent changes from NPs networks to microspheres networks after the gelation was similar to normal micro-syneresis. However, in-situ composition evolution results indicate that the SA is driven by interparticle dehydration, but not affinity difference between the network for itself and for the solvent. In-situ small-angle X-ray scattering (SAXS), UV−vis−NIR, and electric conductivity were used to study the microsyneresis process. To further demonstrate the mechanism, extra complexant was added and successfully restrained the NPs−microsphere transition by inactivating the surface hydroxyl of the NPs. Considering the structural similarity, this work may provide a new approach to control the assemblies of diverse oxide-based NPs.
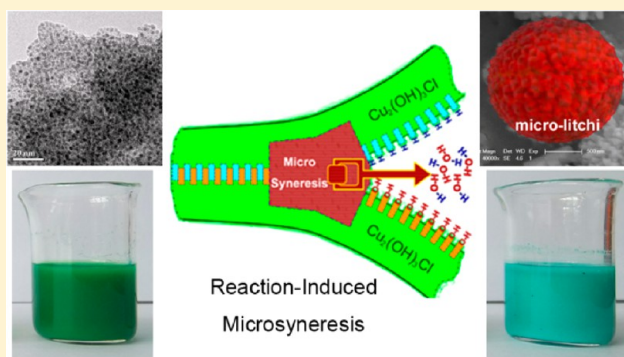
1. INTRODUCTION

Self-assembly (SA) is a common phenomenon existing everywhere but widely studied in modern times. In the broad sense, the formation of the structures in micro scale (atom, molecular, crystal), macro scale (galaxy, star, nebula), or meso scale (organelle, organ, nanostructure) may result from the self-assembly.[1] Among them, mesoscopic self-assembly is compli-cated and diversified but easy to realize in the laboratory. The mesoscopic chemical self-assembly could be facilely controlled by adjusting the synthetic parameters via the chemical reactions, which may help us glance at the self-assembly processes in the other scales.

Also, cross-scale chemical SA has aroused many interests. Conventionally, chemical SA studies focus on the transition from molecules to nanoscale assemblies. Various hierarchical structures have been obtained by hierarchical self-assembly.[2−4] But recently, researchers began to have interests in the assembly process from nanoassemblies (NAs, especially for nanoparticles, NPs) to higher level architectures. Large-scale metal NPs (mostly Au as the building block) assemblies such as crystal, polymer, and diverse helices have been obtained via the inducing of functional polymers (mostly DNA).[5−8] Lately, Orbach et al. further achieved the control of fluorinated-arene or arene induced assembly of gold NPs by simply setting the environmental conditions.[9] The basic idea is to cap noble metal NPs with active groups and cross-link them with other active molecules.

Microsyneresis is the "spontaneous shrinking of a gel with exudation of liquid" (IUPAC definition of "syneresis") "from

microscopic regions".[10] For a nanostructured gel, micro-syneresis is actually a SA process of organizing nanoscale skeletons into higher level objects. Inorganic-based (especially for oxide) NAs commonly possess nanoscale microstructure and active surface hydroxyls, which could be directly assembled without the use of capping agents. Thus, it is relatively facile and low-cost for inorganic-based NAs to achieve a high-level SA in comparison with novel metal NPs. However, the micro-syneresis was observed rarely in inorganic-based gels but often in organic gels.[11−13] Instead of microsyneresis, macroscopic syneresis commonly occurs probably because the inorganic skeletons are usually rigid and inflexible.

In this paper, noncapped oxide-based NPs networks were assembled into litchi-like microsphere networks via a reaction-induced microsyneresis. The microsyneresis occurred in the aging process but was not accompanied by the gelation. The mechanism of assembly process was studied and applied to control the transition from NPs to hierarchical networks (three-level microstructure) by simply adjusting the reactant ratio.

2. EXPERIMENTAL SECTION

2.1. Preparation of Cu$_2$(OH)$_3$Cl Microsphere Networks. Cu(II)-based gel was prepared from cupric chloride (CuCl$_2$·2H$_2$O), poly(acrylic acid) (30 wt % PAA aqua solution, the average molecular weight is 3000), and propylene oxide (PO, 1,2-epoxypropane) via the dispersed inorganic sol−gel (DIS) method. The poly(acrylic acid)
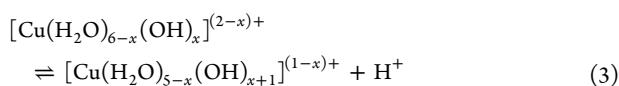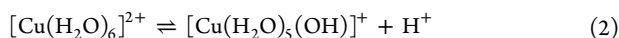
(analytically pure) was purchased from Aladdin Chemistry Company, China. All the other reagents used are analytically pure and provided by Sinopharm Chemical Reagent Co. Ltd., China.

Like the processes reported in previous studies,[14,15] deionized water, poly(acrylic acid) (PAA), and propylene oxide (PO) were successively added into $CuCl_2$−ethanol solution to facilitate the gelation via a sol−gel process. The PAA here acts as both the dispersant and template, and the PO acts as the gelation accelerator.[15,16] The copper(II) compound could gel solely without adding any polymer.[17] 1.032 g of $CuCl_2 \cdot 2H_2O$ was dissolved in 10 mL of ethanol to form a brown solution. After that, 0.65 mL of deionized water was added in to make the solution green. Then 0.77 mL of 30 wt % PAA solution was put into the mixture under magnetic stirring to form slightly bright green solution. After stirring for about 10 min, 1.26 mL of PO was added dropwise. Spatially restricted (by PAA) nucleation and growth began to produce oxide-based NPs via a mild proton-consumption reaction induced by ring-opening nucleophilic addition of PO (sol).[16] Similar to the other cases of the surfactant-induced colloid systems, homogeneous gelation occurred subsequently.[18,19] The sol gradually became an ivy-green and translucent gel after about 2 min (fresh gel). Then the fresh gel was capped and directly aged for about 12 h at room temperature. During aging process, the fresh gel turned cyan, faded out, and became turbid without apparent shrinkage. The aged gel was a light cyan and opaque monolith. The photographs of $CuCl_2$ ethanol solution, $CuCl_2$ ethanol−water solution, $CuCl_2$/PAA ethanol−water solution, fresh gel, and aged gel are presented in Figure S1. At last, the xerogel was obtained by drying the aged gel at room temperature for about one month. The sample became slightly darker and shrank tremendously (more than 60% linear shrinkage) but maintained a monolithic shape. Apparently, the xerogel is obviously more rigid and stable than the aerogel with only a nanoskeleton. A nanoskeleton aerogel is easy to be broken even under a slightly inhomogeneous touch,[15] while a hierarchical xerogel could bear with machining (see section 2.3, the description about the sample preparation for small-angle X-ray scattering characterization).

The colloid is formed via the reactions below.[20] The copper(II) salt in a water-contained solution mainly exists in the form of hydrated ion via a hydration reaction, as seen in formula 1.

$$Cu^{2+} + 6H_2O \rightarrow [Cu(H_2O)_6]^{2+} \tag{1}$$
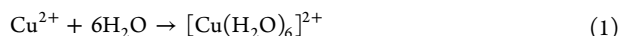
The hydrolysis reactions of hydrated copper ion take place spontaneously, as shown in formulas 2 and 3. The reaction produces hydrogen ion and makes the solution partial acidic.

$$[Cu(H_2O)_6]^{2+} \rightleftharpoons [Cu(H_2O)_5(OH)]^+ + H^+ \tag{2}$$

$$[Cu(H_2O)_{6-x}(OH)_x]^{(2-x)+}$$
$$\rightleftharpoons [Cu(H_2O)_{5-x}(OH)_{x+1}]^{(1-x)+} + H^+ \tag{3}$$

The PO could consume hydrogen ions slowly via a ring-opening nucleophilic addition reaction (formula 4). Thus, the hydrolysis balance turns right and lead to gelation after adding the epoxide.

(4)
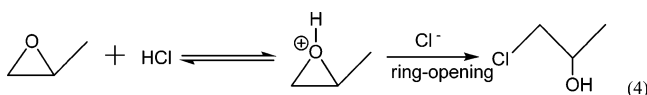
In summary, PO induces the phase separation of $Cu_2(OH)_3Cl$ in the solution, as shown in formula 5.

(5)
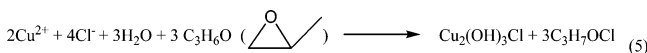
The condensation reaction connects two cupric atoms via oxo or hydroxyl bridge, as shown in formulas 6 and 7. It is worth noting that the other ions like hydroxide ions or chloride ions may affect the condensation reaction, but it is not discussed in this article. Condensation reaction is the fundamental of the nucleation and growth of the colloid particles.

$$-Cu-OH + HO-Cu- \rightarrow -Cu-O-Cu-+H_2O \tag{6}$$

$$-Cu-OH + -Cu- \rightarrow -Cu-\overset{H}{\underset{|}{O}}-Cu- \tag{7}$$
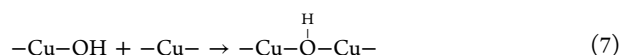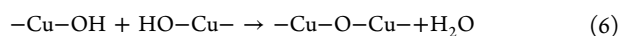
2.2. Reference Experiments.
The reference experiment I (without adding PAA): Similar with the process mentioned above, 1.032 g of $CuCl_2 \cdot 2H_2O$ was dissolved in 10 mL of ethanol to form a brown solution. After that, 0.65 mL of deionized water was added in to make the solution grass-green. Then 1.26 mL of PO was added dropwise. Differently, the precipitate was formed immediately instead of the colloids.

The reference experiment II (controlling the environmental conditions of the aging process): The fresh gels undergoing different temperatures (5, 25, or 50 °C), humidity (about 0, 50, or 100%), and illumination condition (with or without illumination) all faded out and became turbid.

The reference experiment III (to avoid the capillary force via supercritical fluid drying): To avoid the effect of capillary force existing in the natural drying process, CO_2 supercritical fluid drying (SCFD) process was used to treat the aged gel. The details of SCFD are as follows. At first, the aged gel was placed into a stainless autoclave and submerged by ethanol. Then the gel was gradually flushed with liquid CO_2 under the condition of 4 °C and 5 MPa for 3 days to exchange the ethanol with liquid carbon dioxide. After all the ethanol was removed, the autoclave was heated to 42 °C with 0.6 °C/min heating speed and maintained at 42 °C for 4 h. Finally, completely dried gel was obtained by slowly venting off (about 7 bar/h) the autoclave to atmospheric pressure while maintaining the temperature at 42 °C.

The reference experiment IV (to inactivate the surface hydroxyls with 50% more PAA addition): 1.032 g of $CuCl_2 \cdot 2H_2O$ was dissolved in 10 mL of ethanol to form a brown solution. After that, 0.65 mL of deionized water was added in to make the solution grass-green. Then 1.155 mL of 30 wt % PAA solution was put into the mixture under magnetic stirring to form the bright green solution. The gelation occurred after adding 1.26 mL of PO dropwise. Then the bluish-green fresh gel was capped and directly aged for about 12 h at room temperature. During the aging process, no obvious change happened (aged gel).

2.3. Characterizations.
The chemical composition, microstructure, specific surface area and pore distribution, and skeleton fractal structure of the xerogel were characterized by powder X-ray diffraction (XRD, Rigaku D/max2550VB3+/PC), Fourier transform infrared spectroscopy (FTIR, Bruker TENSOR-27), field-emission scanning electron microscopy (FESEM, Philips XL30FEG), high-resolution transmission electron microscopy (HRTEM, JEOL JEM-2011), surface area and pore size analyzer (Quantachrome Autosorb-1-MP), and small-angle X-ray scattering (SAXS, Anton Paar SAXSess-mc2, machining the xerogel monolith into a 1 mm thin slice and wrapping aluminum foil outside the slice for the characterization; the testing time is 60 min). To study the microstructure evolution during the whole sol−gel process, four important states including sol, fresh gel, aged gel, and xerogel were dispersed and stabilized in a large amount of ethanol under ultrasonic vibration for HRTEM characterization to stop the follow-up reactions. Further dilution was adopted in HRTEM sample preparation in order to disperse the sample and avoid the aggregation caused by the drying process.

In addition, the composition or microstructure changes of the fresh gel during the aging process were studied by in-situ FTIR, electrical conductivity meter (Leici DDSJ-308A), UV−vis−NIR double beam spectrometer (Jasco V570), and SAXS. For in-situ FTIR characterization, $CuCl_2$−PAA mixed solution after added PO was injected into the small gap between two silicon wafers for testing. The spectra were recorded at 10 min intervals before 120 min, 20 min intervals from 120 to 180 min, and at 210 min. For electrical conductivity measurement, the probe was direct immersed in the solution, and the data were recorded at 10 s intervals before 5 min, 20 s intervals from 5 to 25 min, 30 s intervals from 25 to 60 min, 60 s intervals from 60 to 120 min, and several minutes intervals after 120 min. For in-situ UV−vis−NIR spectra characterization, a quartz sample cell was placed behind the window of the integrating sphere to test the diffuse reflectance of the colloid sample. The spectra were recorded at 1−4 min intervals before

40 min, 10 min intervals from 40 to 120 min, and 20 min intervals from 120 to 180 min. For SAXS characterization, the $CuCl_2$–PAA mixed solution after added PO was injected into an airtight capillary for testing. The data were recorded (the testing time is 10 min) at 3, 30, 60, and 120 min after adding PO.

3. RESULTS AND DISCUSSION

The xerogel is composed of cross-linked homogeneous microspheres with morphologically rough surface, as shown in Figure 1. Higher resolution field-emission scanning electron
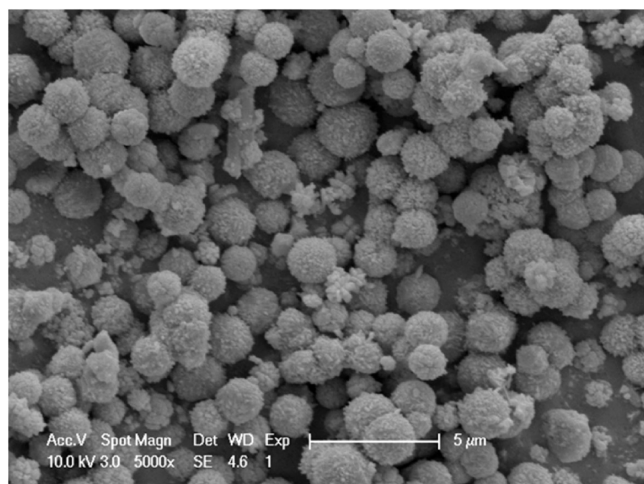

Figure 1. FESEM of the $Cu_2(OH)_3Cl$ xerogel.

microscopy (FESEM) graph (Figure 2g) shows that the microsphere consists of inhomogeneous NPs with the size of several tens of nanometers. As shown in the Figure 2h, there is nanoporous morphology near the edge of the microsphere. In addition, Figure 3 shows that the pore size of the xerogel is narrowly distributed around 3.8 nm, which is an evidence of the existence of the primary structure. That means the xerogel is built up with at least three levels of microstructure with the scales of several nanometers, several tens of nanometers, and submicrometer, respectively.

Powder X-ray diffraction (XRD) and Fourier transform infrared spectroscopy (FTIR) results show that the xerogel is mainly composed of $Cu_2(OH)_3Cl$ and PAA derivatives. As shown in Figure 4, the diffraction peaks match well with the orthorhombic $Cu_2Cl(OH)_3$ (powder diffraction file, PDF card number: 78-0372). Also, as shown in Figure 5, the absorption bands at about 2930, 1705, and 1616 cm^{-1} are attributed to the vibrations of C–H (stretch), C=O (stretch), and HOH (bending), respectively;[15] in the region of 3000–3600 cm^{-1}, the OH stretch vibrations of Cu(II)-based xerogel are divided into two sharp peaks located at 3450 and 3350 cm^{-1}, which may be due to the stretching vibrations of (HO–Cu–)OH and (Cl–Cu–)OH in the $Cu_2(OH)_3Cl$, respectively. These indicate that the xerogel is composed of $Cu_2(OH)_3Cl$ and PAA derivatives. In particular, the bands at 1560 and 1410 cm^{-1} represent the asymmetrical and symmetrical stretching vibrations of COO^-, respectively. The difference of wavenumber is about 150 cm^{-1}, indicating that the interaction between the carboxyl in PAA and the copper ion belongs to the bridge coordination.[15,16,19]

The mesoporous properties were analyzed by using nitrogen adsorption/desorption method. The multipoint specific surface area, total pore volume (the diameter less than 140 nm), and
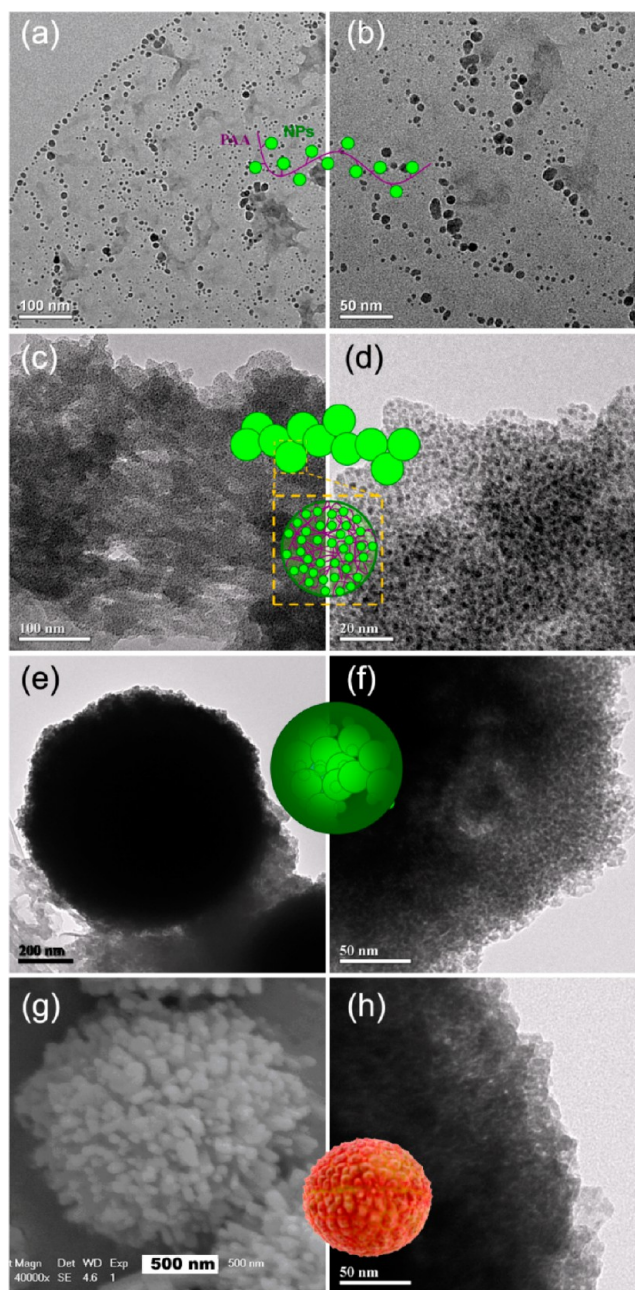

Figure 2. HRTEM graphs of (a, b) sol, (c, d) fresh gel, (e, f) aged gel, (h) and xerogel and FESEM graph of (g) xerogel of $Cu_2(OH)_3Cl$.

average pore diameter of the xerogel are 60.6 m^2 g^{-1}, 0.11 cm^3 g^{-1}, and 7.1 nm, respectively. Surface fractal analysis was made by treating the nitrogen adsorption/desorption results. According to Pfeifer's derivation, gas adsorption in fractal systems is regulated by formula 6[21]

$$V = k\left[\log\left(\frac{P_0}{P}\right)\right]^{D-3}$$

(6)

where V is the total gas volume adsorbed at a given pressure P, k is a material constant, P and P_0 are the equilibrium and saturation pressures of nitrogen adsorbed, and D is the surface fractal dimension.

Based on eq 6, a plot of $\log(V)$ vs $\log[\log(P_0/P)]$ (Frenkel–Halsey–Hill, FHH isotherm, Figure 6) should be a straight line with slope of $(D - 3)$. The FHH isotherm is only valid in the
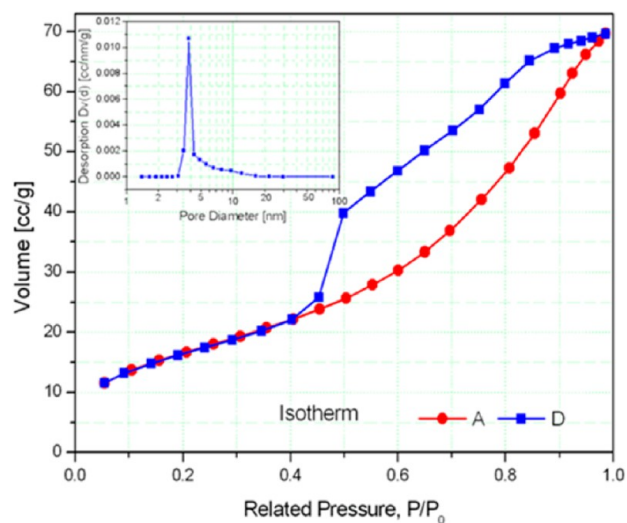
Figure 3. Isotherm and pore-size distribution (inset) of the $Cu_2(OH)_3Cl$ xerogel. Typical hysteresis loop in the nitrogen adsorption/desorption isotherm indicates that the xerogel possesses mesoporous structure. The pore size is narrowly distributed around 3.8 nm, which is an evidence of the primary structure in the xerogel.
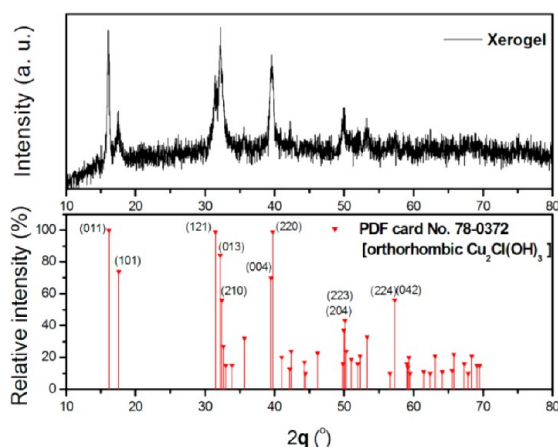
Figure 4. XRD spectrum of the $Cu_2(OH)_3Cl$ xerogel. The peaks match well with the orthorhombic $Cu_2Cl(OH)_3$ (powder diffraction file, PDF card number: 78-0372).
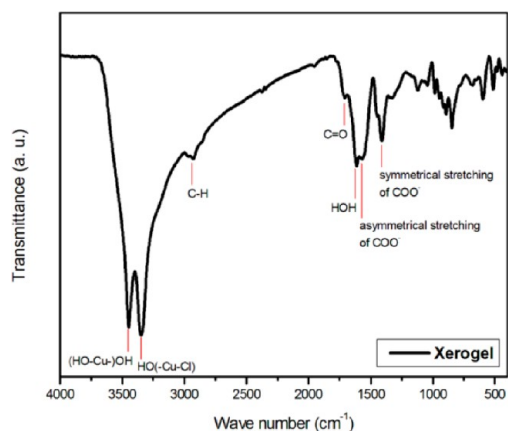
**Figure 5.** FTIR spectrum of the $Cu_2(OH)_3Cl$ xerogel. The xerogel is composed of $Cu_2(OH)_3Cl$ and PAA's derivatives.
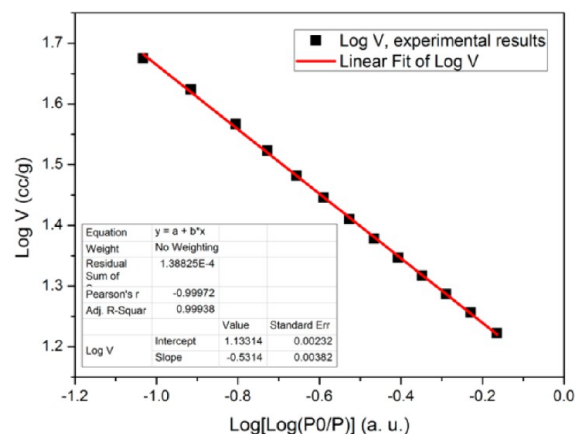
Figure 6. FHH isotherm of $Cu_2(OH)_3Cl$ xerogel. The fractal dimension of the xerogel is calculated to be 2.469 with the correlation coefficient of 0.9997 by analyzing the relative pressure (P_0/P) range from 0.20 to 0.85.

multilayer adsorption mode but not suitable for monolayer adsorption (low-pressure region) or capillary condensation (high-pressure region). Finally, the fractal dimension of the xerogel is calculated to be 2.469 with the correlation coefficient of 0.9997 by analyzing the relative pressure (P_0/P) range from 0.20 to 0.85. As shown in Figure 7, the mass fractal dimension
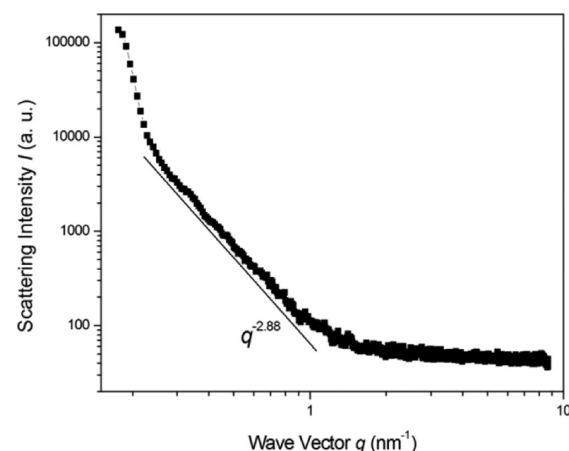
Figure 7. A log–log plot of scattering intensity I versus wave vector q for the $Cu_2(OH)_3Cl$ xerogel. The mass fractal dimension of the xerogel is 2.88.

of the xerogel is 2.88 by linearly fitting the middle wave vector region of scattering intensity versus wave vector curve. It is worth noting that the fractal dimensions calculated by the FHH method and SAXS do not match. This difference may arise from different analysis scales of two methods. The mass fractal dimension region lies on the range about $0.25-1.20$ nm^{-1}, which indicates the fractal exists in the particle size of about several nanometers. The resolution of SAXS is smaller than the size of the primary particles, so that the rough surface in FHH analysis of the xerogel is regarded as smooth in SAXS analysis. The high surface area and fractal dimension indicate that the xerogel has abundant surface and fine microstructure in the nanoscale.

One question puzzled us all the time: why did the fresh gel fade out during aging process? We used to consider the substance change as the reason. However, in-situ FTIR results

showed that there was no obvious difference in chemical composition during aging process.

The structural evolutions were planned to explore this problem by using electron microscopy and in-situ SAXS. However, it was difficult to "capture" the microstructure of the samples in different stages because the sol−gel reactions were so fast that they could not be easily stopped for characterizations. In this paper, we dispersed and stabilized the samples in a large amount of solvent under ultrasonic vibration in order to stop the reactions (following assemblies) by decreasing the concentration of the residual precursor. The samples were further diluted for electron microscopy characterization in order to prevent the nanoarchitectures from aggregation during the dying process (HRTEM sample preparation). Thus, four important states including sol, fresh gel, aged gel, and xerogel were characterized by HRTEM or FESEM. In addition, the changes in color or transparency during sol−gel processes were worth studying to probably reveal the mechanism of SA processes.

The HRTEM graphs exhibit the microstructure of the colloids in different sol−gel stages. The separated NPs in the sol with the size about several nanometers are arranged along the track of branching structure (Figure 2a,b) similar to NPs polymer.[15] As the building block (primary structure) for the follow-up SA, sol NPs are formed via the hydration, hydrolysis, and condensation of copper ion.[16] The wavenumber difference of the xerogel between the absorption bands of asymmetrical and symmetrical stretching vibrations of COO^- group (Figure 5) demonstrates that there is strong coordination interaction between Cu^{2+} ion and carboxyl ligand of PAA, which may guide the nucleation and growth of $Cu_2(OH)_3Cl$.[16,22] The solution turning slightly bright also reveal the coordination (also see in situ UV−vis−NIR spectra). In the reference experiment without adding PAA, precipitation occurred immediately.

The fresh gel exhibits hierarchical microstructure, including a randomly distributed secondary structure with the scale of several tens of nanometers (Figure 2c) and spherical primary NPs with the diameter about 3 nm (Figure 2d). During the gelation, the dispersed NPs in the sol aggregate and form obviously hierarchical (two levels) and coherent skeletons.

However, when undergoing a direct aging process, the secondary particles of the fresh gel aggregate into submicrometer-scale particles with nanoporous morphology (aged gel, Figure 2e,f).

Finally, the xerogel maintains the homogeneous litchi-like morphology (Figures 2g,h and Figure 1). Its secondary NPs become coarsening, which may be induced by crystallization or capillary force.

The microsphere SA occurs in the aging process. The particle size increases from several tens of nanometers to submicrometer scale (similar to the wavelength of visible light), which causes the increase of reflection and scattering of the visible light. That is the reason why the gel faded out and became turbid during the aging process.

The in-situ SAXS characterizations were carried out in an Anton Paar SAXSess-mc2 equipment. The data were recorded at 3, 30, 60, and 120 min after adding PO, respectively. Normally, it is preferred to set the recording time longer than 1 h for a liquid sample. But here, the recording time is only 10 min because the sol−gel reaction is quick. Even so, the recording time seems to be too long. The appearance of the reference sample in a beaker obviously changed during 10 min, especially for the early time (the sol−gel transition happened

for only about 2 min). Better characterizations may be carried out in a synchrotron radiation equipment. As shown in Figure 8, scattering intensity versus wave vector curves indicated that
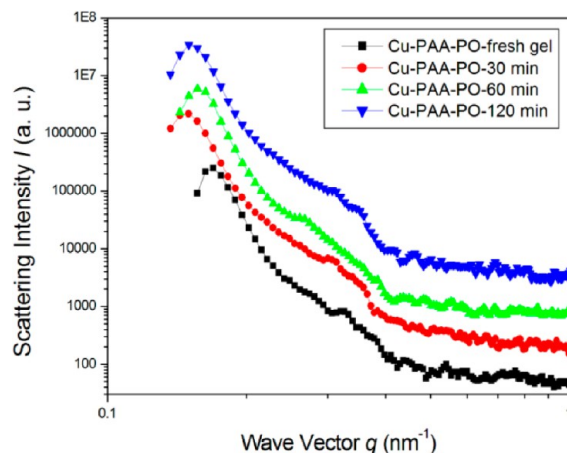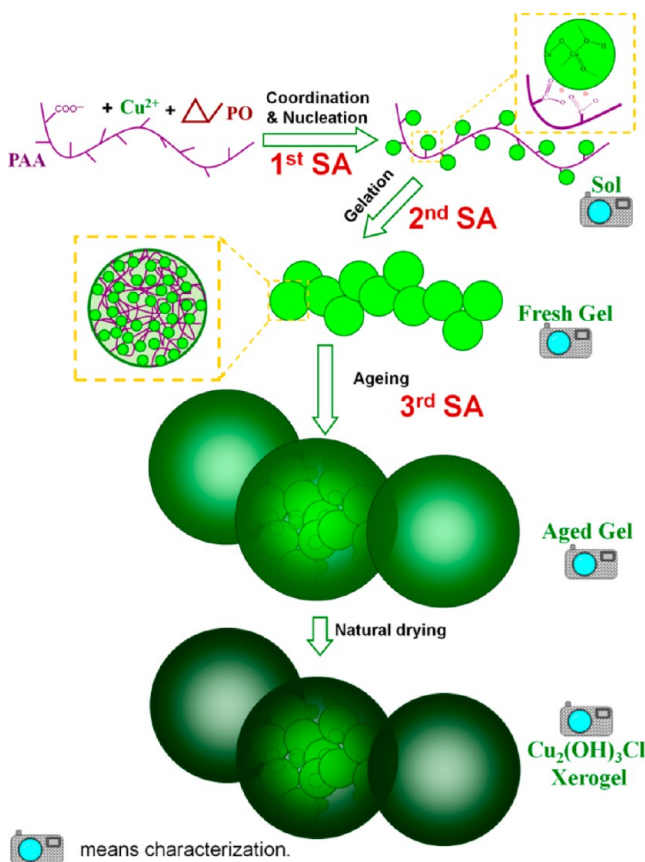

Figure 8. A log−log plot of scattering intensity I versus wave vector q for the wet gel reacted for 3, 30, 60, and 120 min after added PO. To distinguish different curves, the scattering intensities of different samples are multiplied by a coefficient.

the wet gel aged for different times possesses similar nonfractal microstructure in the scale smaller than 100 nm (in the testing range of SAXS). The radius of gyration R_G of the secondary particles (already observed for many kinds of the aerogels) is determined from a Guinier plot. The gel-related systems have a cross-linking, hierarchical, and multidispersed microstructure, which are difficult to be analyzed by adopting a suitable complex model. Because the low q part of $\ln I$ vs q^2 curves near the falling edge of the intensity (Guinier plot) is well linear, and considering that most of references treated aerogel systems by using the Guinier method,[23−29] the Guinier method was chosen to analyze the SAXS data in this paper. Of course, this method may not be strictly accurate in quantity, but the increase or decrease of the particle size should be correct. In our data, the low q part of $\ln I$ vs q^2 curves near the falling edge of the intensity (Guinier plot) is well linear, making this method reliable (see Figure S2). Assuming uniform spheres, the corresponding secondary particle diameter is taken to be equal to $2R_G(5/3)^{0.5}$. According to these equations, the secondary particle diameter of the wet gel reacted for 3, 30, 60, and 120 min are 28.7 ± 1.7, 29.5 ± 1.1, 32.4 ± 0.67, and 30.2 ± 1.0 nm, respectively. In accordance with the HRTEM results (Figure 2c,f), the secondary particles are formed in the fresh gel (gel reacted for 3 min) and remain during the aging process. The secondary particle size increases before 60 min after added PO and slightly decreases subsequently, which may be caused by continuing assembly of the secondary particles and interparticle cross-linking of the primary particles, respectively. Furthermore, the plot of $I \times q^4$ versus q allows the primary particle size to be estimated when possible. However, for all the gel samples, no horizontal asymptote can be observed in the $I \times q^4$ versus q curves (Figure S3), indicating that the primary particle size is too small to detect in this test condition.[29] In addition, the structure larger than 100 nm cannot be analyzed in SAXS spectra, so that the morphology and other studies seem to be necessary.

As shown in Scheme 1, there are three structural evolution procedures in the whole sol−gel process, including sponta-

Scheme 1. Synthesis Route to Cu$_2$(OH)$_3$Cl Microlitchi Networks via Hierarchical Self-Assembly

means characterization.

Figure 9. XRD spectra of the copper(II)-based sol, fresh gel, and aged gel.

neous assembly of sol NPs, template-directed assembly of nanoscale networks, and the assembly of microsphere. The first two processes have been investigated previously,[15,16] whereas the third phenomenon was rarely mentioned. Common capillary-force-directed assembly could be excluded because the self-assembly occurs in aging but not drying process.[30,31] There are no any liquid–gas interface and accompanying capillary force existing in aging process. Furthermore, the aged gel does not exhibit apparent shrinkage but just becomes turbid (microstructure shrinkage), which is the typical phenomenon of microsyneresis.[10−13] However, microsyneresis is commonly caused by "phase separation in which the polymers cluster together, creating" microscopic "regions of free liquid; the driving force is the greater affinity of the polymer for itself than for the pore liquid".[32] Here neither inorganic polymer nor solvent is changed.

Since the particle size increase may only lead to the slight change of the affinity, the reasonable driving force of the microsyneresis was not clear. The microsyneresis was obviously not induced by the affinity change between skeleton and solvent because both of them were not obviously changed. Also, it seemed to be irrelevant to environmental conditions including temperature, humidity, and illumination. We used to suppose that the SA of the microsphere was driven by the capillary force during the natural drying process. However, by adopting supercritical fluid drying to avoid the capillary force, the microspheres were still formed, as shown in Figure S4. Nanoscale crystallization is another usual driving force for the self-assembly. As shown in the Figure 9, no obvious crystallization occurs during the whole sol–gel process,
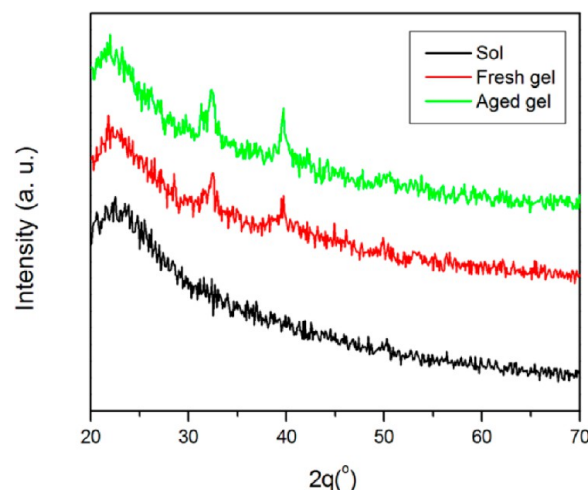
including the aging process. The crystallization of the xerogel must happen in the ambient drying process. Thus, the crystallization should not be the main driving force of the third self-assembly.

The fine spectrum of in-situ FTIR was used to study the slight change of bonds or groups in aging process. In-situ FTIR spectra demonstrate that there are free water increase and Cu-containing compound increase during aging process. The band at about 1625 cm^{-1} normally results from the bending vibration mode of the water.[15] As shown in Figure 10a,c, the peak areas at about 1625 cm^{-1} increase after adding PO for 50 min, which indicates that dehydration reaction occurs in aging process (gelation accomplishes 2 min later after adding PO).

In addition, as shown in Figure 10b, after adding PO for 50 min, the absorption bands between 520 and 420 cm^{-1}, which ascribe to the vibrations of copper–oxygen-related bonds,[33] all increase. The simultaneous dehydration and Cu−O-related bonds increase, indicating that there is the dehydration-induced condensation in the aging process. Moreover, the slight shift of the Cu−O bond from 441 to 444 cm^{-1} implies the changes in lattice parameters caused by the increase of the primary particle size.[33] The dehydration reaction and particle size increase are almost simultaneous, indicating the microlitchi SA is driven by the condensation of the surface hydroxyl groups. Close parts of the gel skeletons are cross-linked first, and subsequently the sections near the cross-linking part get closer and cross-linked under deformation stress of the skeletons. Other parts of the skeletons are then cross-linked gradually during aging process. Finally, the dehydration effect "zips" the NPs up to assemble into litchi-like microsphere networks (see the inset of Figure 10).

There are several times of color changes in this experiment. Thus, the in-situ UV−vis−NIR spectrum (diffuse reflection) was used to characterize the diffuse reflection spectra of the sample. As shown in Figure 11a, the diffuse reflectivity peak of CuCl$_2$ ethanol−water solution lies on the wavelength about 550 nm (green), which is assigned to the absorption of [Cu(H$_2$O)$_6$]$^{2+}$. After adding PAA, a blue-shift of the spectral peak position to about 534 nm is observed, indicating the formation of the coordination between copper ion and carboxyl group in PAA, in accordance with the FTIR results. After adding PO, a blue shift (to about 528 after added PO for 4 min, as shown in Figure 11b) continues and the reflectivity increases
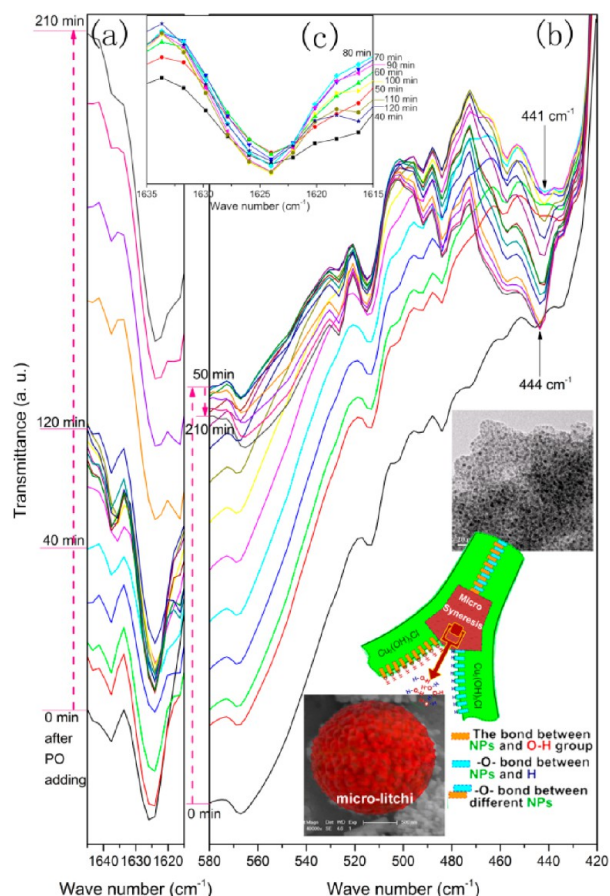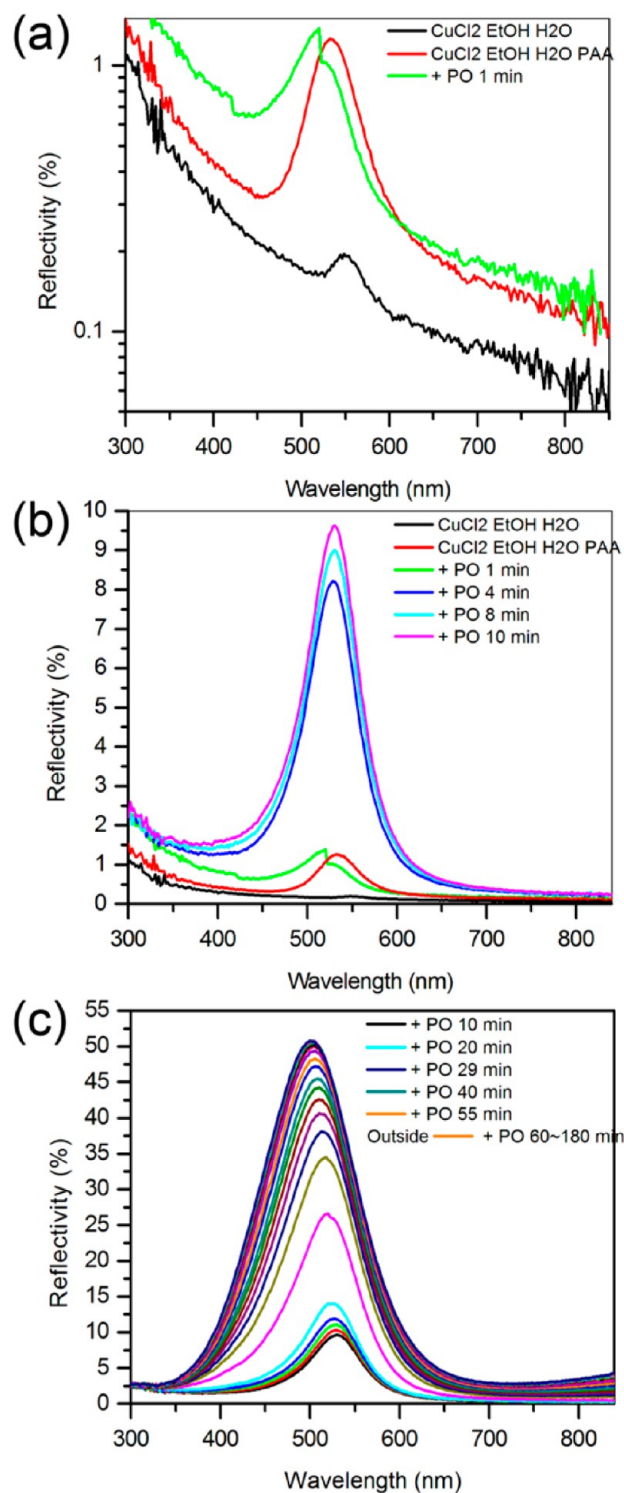
Figure 10. In-situ FTIR spectra of the copper(II)-based colloid during aging process: the spectra in the region of (a) 1645−1615 cm^{-1}, (b) 580−420 cm^{-1} during 0−210 min, and (c) 1635−1615 cm^{-1} during 40−120 min. The inset is the supposed transition process of the microsyneresis.

Figure 11. In-situ UV−vis−NIR spectra of the copper(II)-based colloid during aging process: (a) the spectra of CuCl$_2$ ethanol−water solution, the solution after added PAA, and the solution after added PAA and PO; (b) the spectra of the colloid after added PO for 0−10 min; (c) the spectra of the colloid after added PO for 10−180 min.

rapidly from ∼1% (1 min) to ∼10% (10 min), implying the formation of Cu$_2$(OH)$_3$Cl and the phase separation (secondary structure forming). The spectrum of the wet gel after added PO for 1 min records a transition state. During the testing time of 2−3 min, the sample after added PO for 1 min undergoes a sol−gel transition; therefore, the state of the sample changes quickly along with the scanning direction of the UV−vis−NIR spectrum (the decrease of the wavelength). As seen in Figure 11c, the visible light reflection of the sample after added PO for 30 min increase rapidly, revealing the solid component increase and the microsyneresis beginning (submicrometer structure forming). Thus, the gel fades and becomes "white" (reflection increase in the whole visible light region) to our eyes.

Simultaneously, the peak position shifts from 530 to 505 nm gradually between 10 and 60 min and from 505 to 500 nm (cyan or bluish green) between 60 and 120 min. The mechanism of the blue-shift is not clear now, but considering the microstructure evolution, the blue-shift after 60 min is presumably caused by the shrinkage of the secondary microstructure (in accordance with SAXS results).[35]

It can be observed that a slight red-shift from 528 to 530 nm occurs between 4 and 10 min, which may be attributed to the increase of the secondary particle size. But the conclusion that the secondary particle size increases before 60 min in SAXS results does not correspond with the blue shift between 10 and 60 min in UV−vis−NIR spectra. In-situ electric conductivity

characterization was used to test the changes of the ion concentration, given the situation that UV−vis−NIR spectrum responds to the ion but SAXS does not. As shown in Figure 12, the specific conductivity decreases rapidly from ∼3.00 mS cm^{-1} (0 min) to ∼1.50 mS cm^{-1} (40 min) after added PO and decreases gradually after added PO for 50 min. After added PO,
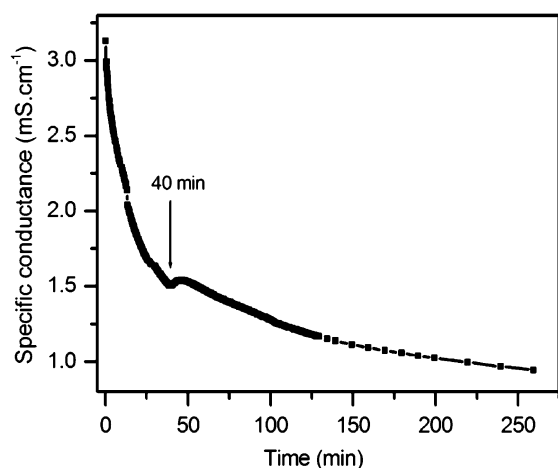
Figure 12. In-situ specific conductivity curve of the copper(II)-based colloid during the aging process.

copper ions and chloride ions decrease to form $Cu_2(OH)_3Cl$ (as shown in formula 5), which leads to the sharp decrease of specific conductivity. It can be observed that the conductivity continues to decrease rapidly after the gelation (reacted for 2 min), indicating that the ions (especially for Cu^{2+}) participate in the aging process (microsyneresis). Moreover, the increase of $Cu_2(OH)_3Cl$ and the decrease of copper ion concentration presumably increase the low wavelength reflection and decrease the high wavelength reflection, respectively, leading to an obvious blue-shift in UV−vis−NIR spectra. There is a conductivity increase in the region of 40−120 min, which attributes to the increase of the ionic mobility under the action of released water (also detected in FTIR spectra).

Therefore, the dehydration reaction of the surface hydroxyls induces the microsyneresis of the oxide-based secondary particles. As presented in Scheme 2, the interparticle cross-linking occurs via simultaneous dehydration of the hydroxyl groups and formation of Cu−O-based bonds outside the different particles. The Cu^{2+} ions may be involved in this reaction to assist the indirect cross-linking far away from the initial cross-linking point. Under the tensile stress raised from the indirect cross-linking, the skeletons may deform and tend to get closer, promoting the subsequent cross-linking. Here the "particle" refers to either secondary particle or primary particle. To secondary particles, the cross-linking is the third SA process (microsyneresis, "zipping" process), while to primary particles, the cross-linking is the driving force of slight decrease of secondary particle size (in accordance with the SAXS data).

Thus, the key factor of controlling the microsphere SA is to inactivate the surface hydroxyl. To further demonstrate the mechanism, 50% more PAA was added in the precursor solution to react with the surface hydroxyls of secondary particles. As shown in the Figure S5, the aged gel adding 50% more PAA maintains the morphology of cross-linked NPs,

which means that the transition from the cross-linked NPs to hierarchical microspheres is restrained. The excess PAA presumably cap the cross-linked NPs to prevent them from condensation and simultaneously disperse them via the electrostatic repulsion of surface carboxylate ions.

4. CONCLUSION

$Cu_2(OH)_3Cl$ NPs-assembled microspheres networks were prepared via hierarchical self-assembly processes. These networks are much more rigid and stable than the aerogel with only nanoskeleton. Among the SA processes, NPs−microsphere SA made the colloid turbid without apparent shrinkage via the microsyneresis. The structure (electron microscope and in-situ SAXS) and composition (in-situ FTIR spectra) evolutions demonstrate that the transition occurs in aging process (the third-level assembly), accompanied by the increase of free water and Cu−O-related bonds. That means the microsyneresis is driven by interparticle dehydration. Furthermore, time-evolution electric conductivity measurement indicates that copper ion may assist the microsyneresis process. At last, the transition was restrained by simply inactivating the surface hydroxyls of NPs. Since the oxide-based NPs have the similar structure of the electric double layers and hydroxyl-capped surface, this work has broad sense to control the assemblies of the other kinds of oxide-based NPs by simply adjusting the reactivity of the surface hydroxyls.

■ ASSOCIATED CONTENT

ⓢ Supporting Information
Photographs of the samples; additional FESEM and HRTEM results. This material is available free of charge via the Internet at http://pubs.acs.org.

■ AUTHOR INFORMATION

Corresponding Author
*E-mail duai@tongji.edu.cn (A.D.), zhoubin863@tongji.edu.cn (B.Z.); Fax +86 21 6598 6071; Tel +86 21 6598 2762.
Notes
The authors declare no competing financial interest.

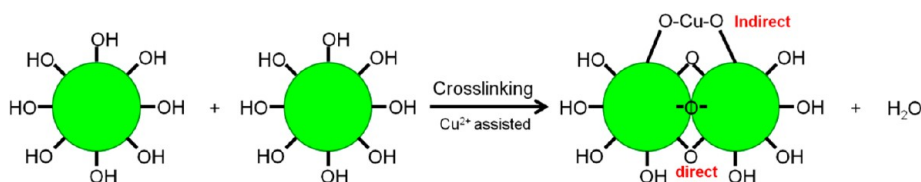## ■ ACKNOWLEDGMENTS

■ REFERENCES

(1) Whitesides, G. M.; Grzybowski, B. Self-assembly at all scales. *Science* **2002**, *295*, 2418−2421.
(2) Amatani, T.; Nakanishi, K.; Hirao, K.; Kodaira, T. Monolithic periodic mesoporous silica with well-defined macropores. *Chem. Mater.* **2005**, *17*, 2114−2119.

Scheme 2. The Supposed Mechanism of the Cross-Linking Process Induced by Interparticle Dehydration

(3) Nakanishi, K.; Kobayashi, Y.; Amatani, T.; Hirao, K.; Kodaira, T. Spontaneous formation of hierarchical macro-mesoporous ethane-silica monolith. *Chem. Mater.* **2004**, *16*, 3652−3658.

(4) Zhang, H. G.; Zhu, Q. S.; Zhang, Y.; Wang, Y.; Zhao, L.; Yu, B. One-pot synthesis and hierarchical assembly of hollow Cu_2O microspheres with nanocrystals-composed porous multishell and their gas-sensing properties. *Adv. Funct. Mater.* **2007**, *17*, 2766−2771.

(5) Aldaye, F. A.; Palmer, A. L.; Sleiman, H. F. Assembling materials with DNA as the guide. *Science* **2008**, *321*, 1795−1799.

(6) Kuzyk, A.; Schreiber, R.; Fan, Z. Y.; Pardatscher, G.; Roller, E. M.; Hogele, A.; Simmel, F. C.; Govorov, A. O.; Liedl, T. DNA-based self-assembly of chiral plasmonic nanostructures with tailored optical response. *Nature* **2012**, *483*, 311−314.

(7) Macfarlane, R. J.; Lee, B.; Jones, M. R.; Harris, N.; Schatz, G. C.; Mirkin, C. A. Nanoparticle superlattice engineering with DNA. *Science* **2011**, *334*, 204−208.

(8) Lin, Y.; Boker, A.; Skaff, H.; Cookson, D.; Dinsmore, A. D.; Emrick, T.; Russell, T. P. Nanoparticle assembly at fluid interfaces: Structure and dynamics. *Langmuir* **2005**, *21*, 191−194.

(9) Orbach, M.; Lahav, M.; Milko, P.; Wolf, S. G.; van der Boom, M. E. Setting the environmental conditions for controlling gold nanoparticle assemblies. *Angew. Chem., Int. Ed.* **2012**, *51*, 7142−7145.

(10) McNaught, A. D.; Wilkinson, A. *Compendium of Chemical Terminology*; Blackwell Science Oxford: Cambridge, UK, 1997; Vol. *1669*.

(11) Fujimura, Y.; Tada, T.; Iino, M. Anisotropic Young's modulus on magnetically ordered agarose gel. *J. Appl. Phys.* **2008**, *104*, 123526 1−4.

(12) Gommes, C. J.; Pirard, J. P.; Goderis, B. Condensation-induced decrease of small-angle X-ray scattering intensity in gelling silica solutions. *J. Phys. Chem. C* **2010**, *114*, 17350−17357.

(13) Charlionet, R.; MachourMerlet, N.; Leclerc, S.; Malandain, J. J. Oriented macroporous polyacrylamide gels. *Electrophoresis* **1997**, *18*, 1133−1135.

(14) Bi, Y. T.; Ren, H. B.; Chen, B. W.; Chen, G.; Mei, Y.; Zhang, L. Synthesis monolithic copper-based aerogel with polyacrylic acid as template. *J. Sol-Gel Sci. Technol.* **2012**, *63*, 140−145.

(15) Du, A.; Zhou, B.; Shen, J.; Xiao, S. F.; Zhang, Z. H.; Liu, C. Z.; Zhang, M. X. Monolithic copper oxide aerogel via dispersed inorganic sol-gel method. *J. Non-Cryst. Solids* **2009**, *355*, 175−181.

(16) Du, A.; Zhou, B.; Shen, J.; Gui, J. Y.; Zhong, Y. H.; Liu, C. Z.; Zhang, Z. H.; Wu, G. M. A versatile sol-gel route to monolithic oxidic gels via polyacrylic acid template. *New J. Chem.* **2011**, *35*, 1096−1102.

(17) Sisk, C. N.; Hope-Weeks, L. J. Copper(II) aerogels via 1,2-epoxide gelation. *J. Mater. Chem.* **2008**, *18*, 2607−2610.

(18) Kanamori, K.; Nakanishi, K. Controlled pore formation in organotrialkoxysilane-derived hybrids: from aerogels to hierarchically porous monoliths. *Chem. Soc. Rev.* **2011**, *40*, 754−770.

(19) Kido, Y.; Nakanishi, K.; Miyasaka, A.; Kanamori, K. Synthesis of monolithic hierarchically porous iron-based xerogels from iron(III) salts via an epoxide-mediated sol-gel process. *Chem. Mater.* **2012**, *24*, 2071−2077.

(20) Du, A.; Zhou, B.; Zhang, Z. H.; Shen, J. A special material or a new state of matter: a review and reconsideration of the aerogel. *Materials* **2013**, *6*, 941−968.

(21) Pfeifer, P.; Wu, Y.; Cole, M.; Krim, J. Multilayer adsorption on a fractally rough surface. *Phys. Rev. Lett.* **1989**, *62*, 1997−2000.

(22) Du, A.; Zhou, B.; Zhong, Y. H.; Zhu, X. R.; Gao, G. H.; Wu, G. M.; Zhang, Z. H.; Shen, J. Hierarchical microstructure and formative mechanism of low-density molybdena-based aerogel derived from $MoCl_5$. *J. Sol-Gel Sci. Technol.* **2011**, *58*, 225−231.

(23) Glatter, O.; Kratky, O. *Small Angle X-ray Scattering*; Academic Press: London, 1982.

(24) Tamon, H.; Ishizaka, E. SAXS study on gelation process in preparation of resorcinol-formaldehyde aerogel. *J. Colloid Interface Sci.* **1998**, *206*, 577−582.

(25) Wang, J.; Shen, J.; Zhou, B.; Wu, X. SAXS investigation of silica aerogels derived from TEOS. *Nanostruct. Mater.* **1996**, *7*, 699−708.

(26) Reichenauer, G.; Emmerling, A.; Fricke, J.; Pekala, R. W. Microporosity in carbon aerogels. *J. Non-Cryst. Solids* **1998**, *225*, 210−214.

(27) Bock, V.; Emmerling, A.; Fricke, J. Influence of monomer and catalyst concentration on RF and carbon aerogel structure. *J. Non-Cryst. Solids* **1998**, *225*, 69−73.

(28) Berthon, S.; Barbieri, O.; Ehrburger-Dolle, F.; Geissler, E.; Achard, P.; Bley, F.; Hecht, A. M.; Livet, F.; Pajonk, G. M.; Pinto, N.; Rigaci, A.; Rochas, C. DLS and SAXS investigations of organic gels and aerogels. *J. Non-Cryst. Solids* **2001**, *285*, 154−161.

(29) Rigacci, A.; Ehrburger-Dolle, F.; Geissler, E.; Chevalier, B.; Sallee, H.; Achard, P.; Barbieri, O.; Berthon, S.; Bley, F.; Livet, F.; Pajonk, G. M.; Pinto, N.; Rochas, C. Investigation of the multi-scale structure of silica aerogels by SAXS. *J. Non-Cryst. Solids* **2001**, *285*, 187−193.

(30) Breen, T. L.; Tien, J.; Oliver, S. R. J.; Hadzic, T.; Whitesides, G. M. Design and self-assembly of open, regular, 3D mesostructures. *Science* **1999**, *284*, 948−951.

(31) Duan, H. G.; Berggren, K. K. Directed self-assembly at the 10 nm scale by using capillary force-induced nanocohesion. *Nano Lett.* **2010**, *10*, 3710−3716.

(32) Brinker, C. J.; Scherer, G. W. *Sol-Gel Science: The Physics and Chemistry of Sol-Gel Processing*; Academic Press: San Diego, CA, 1990.

(33) Kannan, R.; Mohan, S. FTIR study of cerium doped electron superconductors $R_{1.85}Ce_{0.15}CuO_4$ (R = Nd, Pr, Sm, Eu and Gd). *Talanta* **2001**, *53*, 733−739.

(34) Shan, W. J.; Shen, W. J.; Li, C. Structural characteristics and redox behaviors of $Ce_{1-x}Cu_xO_y$ solid solutions. *Chem. Mater.* **2003**, *15*, 4761−4767.

(35) Li, X. Y.; Shen, J.; Du, A.; Zhang, Z. H.; Gao, G. H.; Yang, H. Y.; Wu, J. D. Facile synthesis of silver nanoparticles with high concentration via a CTAB-induced silver mirror reaction. *Colloids Surf., A* **2012**, *400*, 73−79.